

Viscous Hall effect in graphene superlattice enabled via proximity screening

San Kim^{1,*}, Sang Hyeon Park^{1,*}, Sang Il Ahn¹, Shuigang Xu^{2,3}, Kenji Watanabe⁴, Takashi Taniguchi⁵, and Minsoo Kim^{1,†}

¹Department of Physics, Sogang University, Seoul, South Korea

²Key Laboratory for Quantum Materials of Zhejiang Province, Department of Physics, School of Science, Westlake University, Hangzhou, China

³Institute of Natural Sciences, Westlake Institute for Advanced Study, Hangzhou, China

⁴Research Center for Electronic and Optical Materials, National Institute for Materials Science, Tsukuba, Japan

⁵Research Center for Materials Nanoarchitectonics, National Institute for Materials Science, Tsukuba, Japan

*These authors contributed equally to this work

†Correspondence and requests to: minsoo@sogang.ac.kr

Abstract

In electronic systems with strong electron-electron interactions, charge carriers can exhibit fluid-like behavior governed by viscosity. While such hydrodynamic regimes have been observed in pristine graphene, realizing similar behavior in moiré superlattices has been challenging due to enhanced momentum-relaxing umklapp electron-electron scattering. Here, we show that placing a graphene/hBN superlattice in close proximity to a conductive screening layer suppresses umklapp momentum relaxation, creating conditions favorable for observation of viscous electron flow. The hydrodynamic response near the first Dirac point remains largely insensitive to the moiré potential, allowing clear observation of the viscous Hall effect and extraction of the electron-electron scattering length. These results identify proximity screening as a practical route to tune scattering processes and enable quantitative measurement of electron viscosity in moiré superlattices. In contrast, transport near the secondary Dirac points is strongly affected by narrow bandwidth, which hinders reliable measurements of viscous Hall effect in this regime. This limitation highlights the need for multi-component hydrodynamic frameworks to describe narrow-bandwidth moiré systems.

Introduction

Electron hydrodynamics has attracted significant attention due to its distinct transport characteristics, which emerge when electron-electron (e-e) interactions dominate momentum relaxation mechanisms [1-3]. Unlike conventional diffusive transport, which is limited by scattering from impurities and phonons, the hydrodynamic regime is characterized by collective viscous electron flow, including Gurzhi effect [4,5], Poiseuille flow profiles [6,7], negative vicinity resistance [8-11], superballistic transport [12,13], viscous Hall effect [14], and the transport of the Dirac fluid [15-17]. Graphene, with its tunable carrier density and exceptional electronic quality, provides an ideal platform for exploring these hydrodynamic phenomena [18-22]. Recent experimental observations confirmed that clear signatures of electron hydrodynamics become measurable when the e-e scattering length (l_{ee}) is smaller than the mean free path (l) set by momentum-relaxing collisions, requiring ultraclean devices

with minimal disorder.

Graphene superlattices, formed in heterostructures with hexagonal boron nitride (hBN) or via twist-induced moiré patterns, have attracted substantial interest due to the rich correlated phenomena emerging from superlattice-induced band structure modifications [23,24]. In particular, the formation of narrow or flat bands in twisted systems enhances e-e interactions, giving rise to correlated insulating phases and superconductivity [25,26]. From a hydrodynamic perspective, such band modifications open compelling opportunities to engineer electron viscosity. Variations in band curvature and local density of states directly affect the Fermi velocity and the phase space available for e-e scattering, which in turn determine l_{ee} and, hence, the viscous response of the system [27,28]. These suggest that hydrodynamic flow in moiré-engineered systems is not only accessible but tunable, enabling systematic exploration of how lattice geometry and electronic correlations shape viscous transport.

Despite their rich band structure, direct observation of electron hydrodynamics in graphene superlattices has remained challenging. Strong umklapp momentum-relaxing e-e scattering significantly reduces the mean free path, driving resistivity to scale with T^2 and hindering the condition ($l_{ee} < l$) necessary for hydrodynamic electron transport [29]. To overcome this limitation, we introduce proximity screening via metallic gates, which suppresses umklapp processes [30], thereby enabling clear hydrodynamic flow in graphene/hBN superlattices. This screening allows us to realize robust viscous behavior, as evidenced by the viscous Hall effect. Remarkably, we find that both electron viscosity and e-e scattering lengths in screened graphene superlattices closely match those of pristine graphene, indicating that the primary barrier to hydrodynamics is the large momentum loss from umklapp scattering. We further examine the dependence of electron viscosity on temperature and charge density, uncovering consistent hydrodynamic characteristics across a range of experimental conditions. Although we observe no significant modifications beyond those attributable to proximity screening, our study suggests screening of strong e-e scattering enables accessing electron hydrodynamics in these moiré heterostructures.

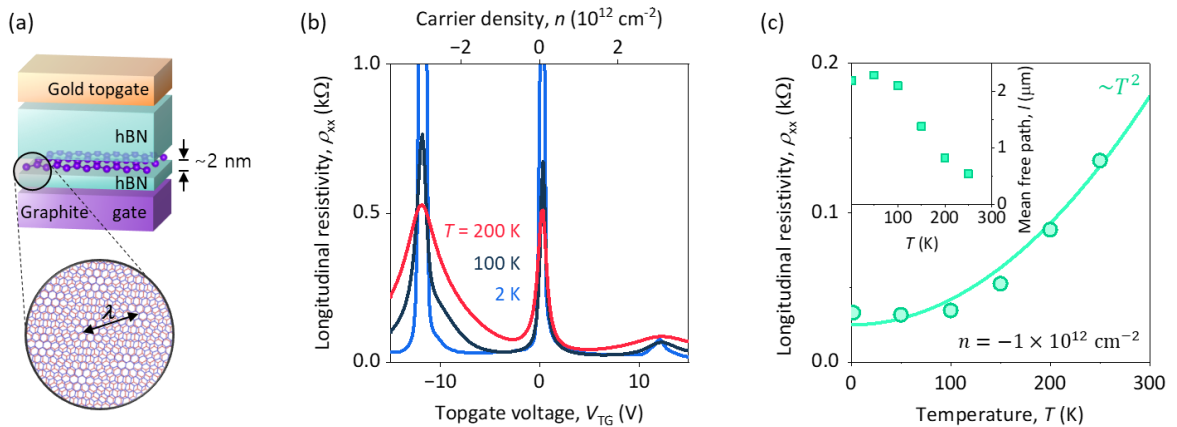


Figure 1 | Electron transport in a proximity-screened graphene/hBN superlattice. **a**, Schematic of the graphene/hBN superlattice device, consisting of monolayer graphene aligned with an encapsulating hBN layer and separated from a metallic graphite backgate by an atomically thin ($\sim 2 \text{ nm}$) hBN spacer. The nearby graphite gate provides strong electrostatic screening, suppressing momentum-relaxing umklapp e-e scattering. **b**, Longitudinal resistivity (ρ_{xx}) versus topgate voltage (V_{TG}) at temperatures of 2, 100, and 200 K. In addition to

the first Dirac point at $V_{TG} = 0$ V, pronounced maxima at $V_{TG} = \pm 12.0$ V mark the secondary Dirac points of the moiré minibands. **c**, Temperature dependence of ρ_{xx} at carrier density $n = -1.0 \times 10^{12} \text{ cm}^{-2}$. The resistivity increase follows a T^2 dependence characteristics of umklapp e-e scattering but with a significantly reduced magnitude compared to unscreened devices, reflecting suppression of long-range Coulomb interactions by proximity screening. Inset: Momentum-relaxing mean free path l extracted at the same carrier density, approaching the device width at low temperature and remaining above ~ 600 nm up to 250 K, thereby satisfying $L \lesssim l$ and enabling hydrodynamic measurements.

Methods

Figure 1a presents a schematic of the graphene/hBN superlattice heterostructure. The superlattice is realized by aligning monolayer graphene with encapsulating hBN layer such that their crystallographic axes match within a small angular mismatch. The graphene sheet is placed atop an atomically thin (2.0 nm) hBN spacer, which separates it from a metallic graphite back gate. This nearby graphite gate serves as a highly effective metallic screen, substantially reducing long-range Coulomb interactions and thereby suppressing momentum-relaxing umklapp e-e scattering [30]. The heterostructure is encapsulated with a top hBN layer, on which a metallic top-gate electrode (Cr/Au) is defined via e-beam processes to enable independent electrostatic control of the carrier density. The completed stack is patterned into a conventional Hall-bar geometry with a channel width $W = 2.0 \mu\text{m}$ and a center-to-center spacing between adjacent voltage probes of $L = 0.6 \mu\text{m}$. These dimensions are particularly suited for probing the viscous Hall effect, as they allow access to the regime in which $l_{ee} < L < l$, a necessary condition for observing electron hydrodynamics.

Results

The formation of the graphene/hBN superlattice is confirmed through electron transport measurements of the longitudinal resistivity (ρ_{xx}) as a function of topgate voltage (V_{TG}) (Fig. 1b). In addition to the first Dirac point at zero gate voltage, pronounced resistivity maxima appear near $V_{TG} = \pm 12.0$ V, corresponding to carrier densities $|n| = 3.0 \times 10^{12} \text{ cm}^{-2}$. These densities correspond to a moiré lattice constant of approximately 12.4 nm, which is consistent with a graphene-hBN crystallographic misalignment angle of $\theta \approx 0.9^\circ$. The identification of these secondary Dirac points is corroborated by Hall sign reversals and Brown-Zak oscillations observed in separate magnetotransport measurements [31], which are well-established signatures of miniband formation. Away from the Dirac points, ρ_{xx} exhibits a moderate but systematic enhancement with temperature, consistent with the activation of momentum-relaxing umklapp e-e scattering in the superlattice minibands.

To examine how proximity screening influences momentum-relaxing processes, Fig. 1c shows the temperature dependence of the longitudinal resistivity $\rho_{xx}(T)$ at a representative carrier density of $n = -1.0 \times 10^{12} \text{ cm}^{-2}$. For quantitative comparison, we define $\Delta\rho_{xx}(T) \equiv \rho_{xx}(T) - \rho_{xx}(2 \text{ K})$, which isolates the channel resistance at base temperature. The extracted $\Delta\rho_{xx}$ follows a T^2 dependence characteristic of umklapp e-e scattering in graphene superlattice. In unscreened devices with a similar lattice constant, $\Delta\rho_{xx}$ at 200 K has been reported to reach approximately 170 Ω at this density [29], whereas in the present device, which incorporates a 2.0 nm hBN spacer between graphene and a metallic graphite backgate, the increase is limited to about 55 Ω . This nearly threefold

reduction reflects the suppression of long-range Coulomb interactions and the corresponding decrease in umklapp e-e scattering rate due to electrostatic screening. The inset of Fig. 1c presents the momentum-relaxing mean free path extracted from the resistivity, which approaches the device width at low temperature, indicating ballistic transport at 2 K. With increasing temperature, l decreases but remains above approximately 600 nm up to 250 K, ensuring that the condition $L \lesssim l$ is satisfied. This places the device in a regime where l_{ee} can be shorter than l , enabling quantitative extraction of l_{ee} from viscous Hall effect measurements discussed in Fig. 2.

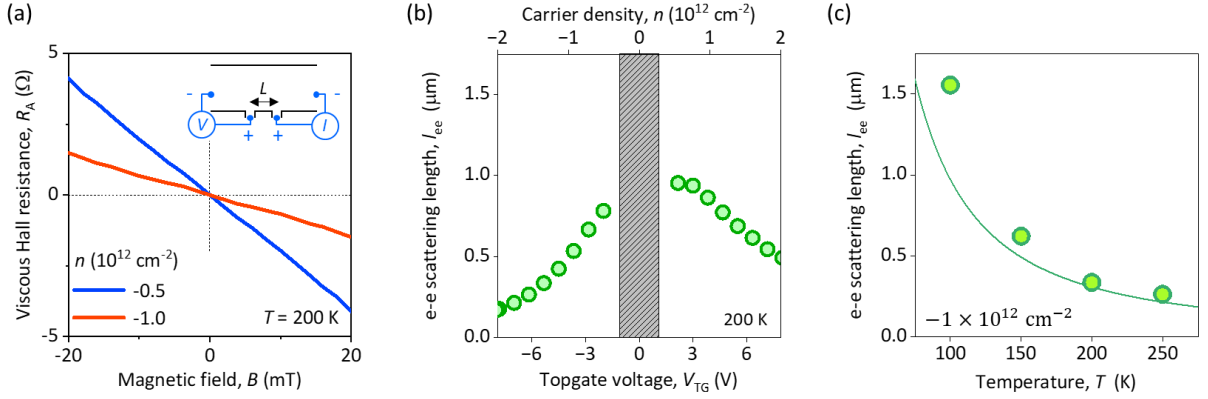


Figure 2 | Electron-electron scattering length extracted from viscous Hall measurements in a graphene/hBN superlattice. **a**, Viscous Hall resistance R_A measured at $T = 200$ K for a representative carrier density $n = -0.5 \times 10^{12}$ (blue) and $-1.0 \times 10^{12} \text{ cm}^{-2}$ (red), using a vicinity geometry configuration. This signal arises from the Hall viscosity and enables quantitative extraction of the e-e scattering length l_{ee} . **b**, Carrier density dependence of l_{ee} at 200 K, showing a gradual decrease in magnitude with increasing density, consistent with more effective Coulomb screening at low densities. The shaded regions near the Dirac points mark density ranges where electron and hole populations coexist, making the single-component hydrodynamic description inapplicable. **c**, Temperature dependence of l_{ee} at $n = -1.0 \times 10^{12} \text{ cm}^{-2}$. The extracted values decrease with increasing temperature, in good agreement with hydrodynamic theory including proximity screening effects.

Viscous Hall effect measurements were performed using the vicinity geometry shown in the right inset of Fig. 2a, where a narrow current injector and a nearby voltage probe ($L = 0.6 \mu\text{m}$) are positioned along one edge of the device. When a perpendicular magnetic field B is applied, the potential distribution near the injector becomes asymmetric due to the Hall viscosity, producing an antisymmetric-in- B contribution to the measured vicinity resistance [14], denoted as the viscous Hall resistance R_A . This contribution is extracted as $R_A = [R_v(B) - R_v(-B)]/2$, which removes the symmetric background from Ohmic and longitudinal viscous flows. Since the Hall viscosity is proportional to the product of n and l_{ee} , this relation enables quantitative extraction of l_{ee} from the measured R_A without requiring any adjustable parameters. Figure 2a presents representative R_A traces at 200 K for $n = -0.5 \times 10^{12}$ and $-1.0 \times 10^{12} \text{ cm}^{-2}$.

The extracted l_{ee} values reveal systematic trends with both carrier density and temperature, as summarized in Figs. 2b and 2c. At a fixed temperature of 200 K, l_{ee} decreases with increasing $|n|$, reflecting stronger e-e scattering at higher densities. This trend is consistent with the expected reduction of the Thomas-Fermi screening length $1/q_{TF}$ at elevated densities, which diminishes the effectiveness of Coulomb screening and enhances interaction-mediated momentum exchange. In a

complementary manner, at a fixed density of $n = -1.0 \times 10^{12}$, l_{ee} exhibits a decreasing trend with increasing temperature. This behavior closely follows the theoretical expectation for screened e-e scattering in a Fermi liquid [30], described by:

$$\ell_{ee} \approx \frac{4\hbar v_F E_F}{\pi} \frac{1}{(k_B T)^2 \ln\left(\frac{2E_F}{k_B T}\right)} \left(\frac{1 + 2dq_{TF}}{2dq_{TF}}\right)^2$$

where \hbar is the reduced Planck constant, k_B is the Boltzmann constant, v_F is the Fermi velocity, E_F is the Fermi energy, and d is the dielectric distance of 2.0 nm. The good agreement between the temperature dependence of the measured l_{ee} and this model confirms that proximity screening plays a key role in shaping e-e interactions. At the low temperatures, however, the extracted values deviate from the theoretical curve, which may be attributed to l approaching the device width, such that ballistic contributions complicate the extraction of l_{ee} from measured R_v [11]. A slight asymmetry between the electron and hole sides is also visible in the data in Fig. 2b, which may arise from differences in umklapp scattering rates on each side [29], as the extraction of l_{ee} involves the measured longitudinal resistivity.

While these measurements are carried out in a graphene superlattice, the overall magnitude and functional dependence of l_{ee} near the first Dirac point are remarkably similar to those reported in monolayer graphene. This agreement arises from the fact that the moiré superlattice primarily modulates the electronic structure near the secondary Dirac points, leaving the low-energy spectrum near the first Dirac point largely unaltered. As a result, the hydrodynamic behavior extracted from our measurements, both in its density and temperature dependence, reflects the same underlying physics previously observed in non-superlattice monolayer devices [30]. This comparison further supports the interpretation that the experimentally extracted l_{ee} follows the screened interaction model, as described in the preceding equation. It also demonstrates that the incorporation of a superlattice does not preclude hydrodynamic behavior in graphene, provided the measurement is conducted in an energy range where the Dirac dispersion remains intact. Thus, proximity screening not only mitigates momentum-relaxing processes but also enables a robust, quantitative window into electron hydrodynamics within superlattice-integrated graphene systems.

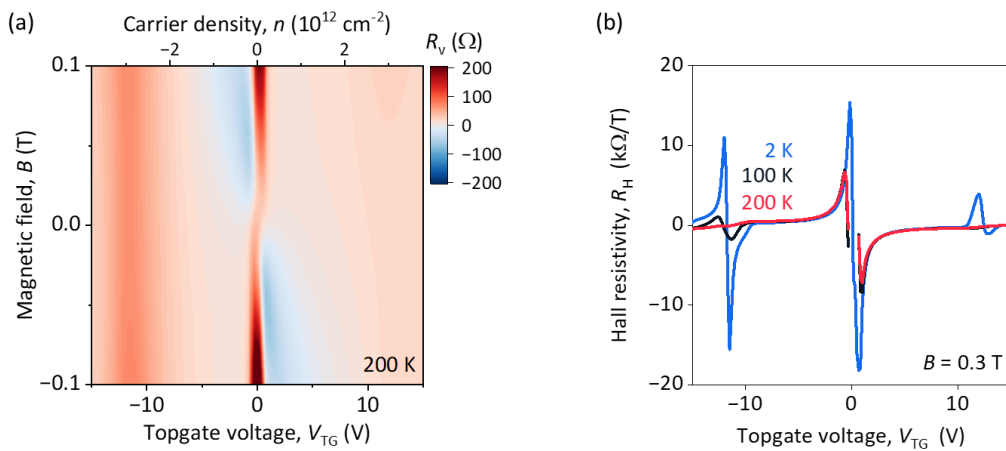


Figure 3 | Breakdown of single-component hydrodynamic description near the secondary Dirac point in a graphene/hBN superlattice. a, Vicinity resistance $R_v(B, V_{TG})$ map measured at $T = 200$ K, illustrating ballistic

transport signatures (negative R_v from magnetic focusing) near the first Dirac point, and the transition to ballistic to diffusive transport near the secondary Dirac point where momentum-relaxing scattering dominates. **b**, Temperature dependence of Hall resistivity R_H as a function of V_{TG} at $T = 2, 100, 200$ K (blue, black, red). The response near the secondary Dirac point changes dramatically due to a thermal excitation in the narrow superlattice miniband. These features indicate that, in this region, both electron and hole contribute to transport, making a single-component hydrodynamic theory inadequate.

To explore the hydrodynamic transport in graphene superlattices, we extend our measurements beyond the carrier density ranges previously discussed and examine the vicinity of the secondary Dirac points. For reliable extraction of viscous Hall resistance, the measurement geometry must support momentum-conserving transport, requiring $l_{ee} < L < l$. Therefore, ballistic transport should be satisfied as a prerequisite, and an effective way to verify this condition in the same vicinity geometry is to observe magnetic focusing [32]. Here, the application of a perpendicular magnetic field modifies electron trajectories such that, when the cyclotron diameter becomes comparable to the probe spacing L , a negative resistance can be observed. The appearance of magnetic focusing thus directly confirms that the inequality $L < l$ holds. Figure 3a presents representative R_v measurements at 200 K near the first and secondary Dirac points. Near the first Dirac point, clear magnetic focusing features are visible, confirming ballistic transport. In this regime, viscous effects manifest near zero magnetic field as antisymmetric contributions to the vicinity resistance R_v , allowing meaningful extraction of the viscous Hall effect. In contrast, magnetic focusing signatures vanish near the secondary neutrality points, indicating that momentum-relaxing scattering dominates. This breakdown renders the extraction of meaningful viscous Hall signals unfeasible in these regions.

The temperature dependence of the Hall resistivity (R_H) further highlights the difficulty of applying single-component hydrodynamic theory near the secondary Dirac points. As shown in Fig. 3b, the Hall resistivity near the first Dirac point ($1 \text{ V} \lesssim |V_{TG}| \lesssim 8 \text{ V}$) remains relatively invariant across temperatures from 2 K to 200 K. However, near the secondary Dirac points ($V_{TG} \approx \pm 12 \text{ V}$), dramatic changes are observed. This sensitivity originates from the narrow bandwidth near secondary Dirac point [23], which amplifies the effect of thermal excitation. Furthermore, while the gate voltage corresponding to the secondary Dirac points remains fixed with temperature, the position of the zero-crossing in R_H shifts substantially, from near -12.0 V at 200 K to -10.2 V at 100 K and -9.4 V at 2 K. This shift is not due to movement of the van Hove singularity itself, which is determined by the band structure, but rather reflects the energy asymmetry of the bands. As the temperature decreases, the thermal distribution of carriers narrows, and the asymmetric density of states causes the electron-hole balance point to shift in gate voltage. These observations suggest that both electron and hole populations contribute simultaneously near the secondary Dirac points and van Hove singularity, particularly at elevated temperatures, precluding the use of single-component hydrodynamic models. A more comprehensive description incorporating two-component transport is likely necessary to accurately capture electron hydrodynamics in this regime [33,34].

Conclusions

In conclusion, we have shown that proximity screening enables the emergence of electron

hydrodynamics in graphene superlattices by suppressing momentum-relaxing umklapp e-e scattering. The extracted electron viscosity and scattering length exhibit density and temperature dependencies consistent with those observed in monolayer graphene, suggesting that electron hydrodynamics near the first Dirac point is largely unaffected by the presence of a moiré potential. In contrast, near the secondary Dirac points, ballistic transport breaks down and the Hall response becomes strongly temperature-dependent due to thermal excitation and asymmetry in the energy bands, rendering single-component electron hydrodynamic models inapplicable. These findings demonstrate that proximity screening in van der Waals heterostructures offers a viable route to access viscous electronic transport by reducing umklapp scattering, but also reveal that the applicability of single-component electron hydrodynamics crucially depends on the underlying band structure. More broadly, in narrow-bandwidth moiré systems such as twisted two-dimensional heterostructures, future studies must account for the interplay between electrons and holes to capture the collective behavior of interacting Dirac fluids.

Acknowledgements

We acknowledge helpful discussions with A. Geim and A. Principi. Half of this research was supported by the Nano and Material Technology Development Program through the National Research Foundation of Korea (NRF) funded by Ministry of Science and ICT (MSIT) (No. RS-2024-00444725). M.K. was supported by the NRF of Korea grant funded by the Korean government (MSIT) (No. RS-2022-NR071693, No. RS-2023-00303081, No. RS-2024-00410027). S.X. was supported by the Zhejiang Provincial Natural Science Foundation of China (XHD23A2001). K.W. and T.T. acknowledge support from the JSPS KAKENHI (Grant Numbers 21H05233 and 23H02052), the CREST (JPMJCR24A5), JST and World Premier International Research Center Initiative (WPI), MEXT, Japan.

References

- [1] A. O. Govorov and J. J. Heremans, Hydrodynamic Effects in Interacting Fermi Electron Jets, *Physical Review Letters* **92**, 026803 (2004).
- [2] A. V. Andreev, S. A. Kivelson, and B. Spivak, Hydrodynamic Description of Transport in Strongly Correlated Electron Systems, *Physical Review Letters* **106**, 256804 (2011).
- [3] P. J. W. Moll, P. Kushwaha, N. Nandi, B. Schmidt, and A. P. Mackenzie, Evidence for hydrodynamic electron flow in PdCoO₂, *Science* **351**, 1061 (2016).
- [4] R. N. Gurzhi, HYDRODYNAMIC EFFECTS IN SOLIDS AT LOW TEMPERATURE, *Soviet Physics Uspekhi* **11**, 255 (1968).
- [5] M. J. M. de Jong and L. W. Molenkamp, Hydrodynamic electron flow in high-mobility wires, *Physical Review B* **51**, 13389 (1995).
- [6] J. A. Sulpizio, L. Ella, A. Rozen, J. Birkbeck, D. J. Perello, D. Dutta, M. Ben-Shalom, T. Taniguchi, K. Watanabe, T. Holder *et al.*, Visualizing Poiseuille flow of hydrodynamic electrons, *Nature* **576**, 75 (2019).
- [7] M. J. H. Ku, T. X. Zhou, Q. Li, Y. J. Shin, J. K. Shi, C. Burch, L. E. Anderson, A. T. Pierce, Y. Xie, A.

- Hamo *et al.*, Imaging viscous flow of the Dirac fluid in graphene, *Nature* **583**, 537 (2020).
- [8] D. A. Bandurin, I. Torre, R. K. Kumar, M. Ben Shalom, A. Tomadin, A. Principi, G. H. Auton, E. Khestanova, K. S. Novoselov, I. V. Grigorieva *et al.*, Negative local resistance caused by viscous electron backflow in graphene, *Science* **351**, 1055 (2016).
 - [9] L. Levitov and G. Falkovich, Electron viscosity, current vortices and negative nonlocal resistance in graphene, *Nature Physics* **12**, 672 (2016).
 - [10] F. M. D. Pellegrino, I. Torre, A. K. Geim, and M. Polini, Electron hydrodynamics dilemma: Whirlpools or no whirlpools, *Physical Review B* **94**, 155414 (2016).
 - [11] D. A. Bandurin, A. V. Shytov, L. S. Levitov, R. K. Kumar, A. I. Berdyugin, M. Ben Shalom, I. V. Grigorieva, A. K. Geim, and G. Falkovich, Fluidity onset in graphene, *Nature Communications* **9**, 4533 (2018).
 - [12] H. Guo, E. Ilseven, G. Falkovich, and L. S. Levitov, Higher-than-ballistic conduction of viscous electron flows, *Proceedings of the National Academy of Sciences* **114**, 3068 (2017).
 - [13] R. Krishna Kumar, D. A. Bandurin, F. M. D. Pellegrino, Y. Cao, A. Principi, H. Guo, G. H. Auton, M. Ben Shalom, L. A. Ponomarenko, G. Falkovich *et al.*, Superballistic flow of viscous electron fluid through graphene constrictions, *Nature Physics* **13**, 1182 (2017).
 - [14] A. I. Berdyugin, S. G. Xu, F. M. D. Pellegrino, R. Krishna Kumar, A. Principi, I. Torre, M. Ben Shalom, T. Taniguchi, K. Watanabe, I. V. Grigorieva *et al.*, Measuring Hall viscosity of graphene's electron fluid, *Science* **364**, 162 (2019).
 - [15] J. Crossno, J. K. Shi, K. Wang, X. Liu, A. Harzheim, A. Lucas, S. Sachdev, P. Kim, T. Taniguchi, K. Watanabe *et al.*, Observation of the Dirac fluid and the breakdown of the Wiedemann-Franz law in graphene, *Science* **351**, 1058 (2016).
 - [16] P. Gallagher, C.-S. Yang, T. Lyu, F. Tian, R. Kou, H. Zhang, K. Watanabe, T. Taniguchi, and F. Wang, Quantum-critical conductivity of the Dirac fluid in graphene, *Science* **364**, 158 (2019).
 - [17] C. Tan, D. Y. H. Ho, L. Wang, J. I. A. Li, I. Yudhistira, D. A. Rhodes, T. Taniguchi, K. Watanabe, K. Shepard, P. L. McEuen *et al.*, Dissipation-enabled hydrodynamic conductivity in a tunable bandgap semiconductor, *Science Advances* **8**, eabi8481 (2022).
 - [18] R. Bistritzer and A. H. MacDonald, Hydrodynamic theory of transport in doped graphene, *Physical Review B* **80**, 085109 (2009).
 - [19] M. Müller, J. Schmalian, and L. Fritz, Graphene: A Nearly Perfect Fluid, *Physical Review Letters* **103**, 025301 (2009).
 - [20] B. N. Narozhny, I. V. Gornyi, M. Titov, M. Schütt, and A. D. Mirlin, Hydrodynamics in graphene: Linear-response transport, *Physical Review B* **91**, 035414 (2015).
 - [21] N. Narozhny Boris, V. Gornyi Igor, D. Mirlin Alexander, and J. Schmalian, Hydrodynamic Approach to Electronic Transport in Graphene, *Annalen der Physik* **529**, 1700043 (2017).
 - [22] M. Polini and A. K. Geim, Viscous electron fluids, *Physics Today* **73**, 28 (2020).
 - [23] M. Yankowitz, J. Xue, D. Cormode, J. D. Sanchez-Yamagishi, K. Watanabe, T. Taniguchi, P. Jarillo-Herrero, P. Jacquod, and B. J. LeRoy, Emergence of superlattice Dirac points in graphene on hexagonal boron nitride, *Nature Physics* **8**, 382 (2012).
 - [24] L. A. Ponomarenko, R. V. Gorbachev, G. L. Yu, D. C. Elias, R. Jalil, A. A. Patel, A. Mishchenko, A. S. Mayorov, C. R. Woods, J. R. Wallbank *et al.*, Cloning of Dirac fermions in graphene superlattices, *Nature* **497**, 594 (2013).

- [25] Y. Cao, V. Fatemi, S. Fang, K. Watanabe, T. Taniguchi, E. Kaxiras, and P. Jarillo-Herrero, Unconventional superconductivity in magic-angle graphene superlattices, *Nature* **556**, 43 (2018).
- [26] Y. Cao, V. Fatemi, A. Demir, S. Fang, S. L. Tomarken, J. Y. Luo, J. D. Sanchez-Yamagishi, K. Watanabe, T. Taniguchi, E. Kaxiras *et al.*, Correlated insulator behaviour at half-filling in magic-angle graphene superlattices, *Nature* **556**, 80 (2018).
- [27] E. Di Salvo, P. Cosme, and L. Fritz, Hydrodynamics in generalized electronic two-band systems, arXiv:2505.21176 (2025).
- [28] A. Hui, C. Pozderac, and B. Skinner, Two-dimensional hydrodynamic electron flow through periodic and random potentials, *Physical Review B* **109**, 155145 (2024).
- [29] J. R. Wallbank, R. Krishna Kumar, M. Holwill, Z. Wang, G. H. Auton, J. Birkbeck, A. Mishchenko, L. A. Ponomarenko, K. Watanabe, T. Taniguchi *et al.*, Excess resistivity in graphene superlattices caused by umklapp electron–electron scattering, *Nature Physics* **15**, 32 (2019).
- [30] M. Kim, S. G. Xu, A. I. Berdyugin, A. Principi, S. Slizovskiy, N. Xin, P. Kumaravadivel, W. Kuang, M. Hamer, R. Krishna Kumar *et al.*, Control of electron-electron interaction in graphene by proximity screening, *Nature Communications* **11**, 2339 (2020).
- [31] R. Krishna Kumar, A. Mishchenko, X. Chen, S. Pezzini, G. H. Auton, L. A. Ponomarenko, U. Zeitler, L. Eaves, V. I. Fal’ko, and A. K. Geim, High-order fractal states in graphene superlattices, *Proceedings of the National Academy of Sciences* **115**, 5135 (2018).
- [32] M. Lee, J. R. Wallbank, P. Gallagher, K. Watanabe, T. Taniguchi, V. I. Fal’ko, and D. Goldhaber-Gordon, Ballistic miniband conduction in a graphene superlattice, *Science* **353**, 1526 (2016).
- [33] N. Xin, J. Lourembam, P. Kumaravadivel, A. E. Kazantsev, Z. Wu, C. Mullan, J. Barrier, A. A. Geim, I. V. Grigorieva, A. Mishchenko *et al.*, Giant magnetoresistance of Dirac plasma in high-mobility graphene, *Nature* **616**, 270 (2023).
- [34] Y. Zeng, H. Guo, O. M. Ghosh, K. Watanabe, T. Taniguchi, L. S. Levitov, and C. R. Dean, Quantitative measurement of viscosity in two-dimensional electron fluids, arXiv:2407.05026 (2024).